



**Environmental
Science**
Water Research & Technology

**Treatment of Emerging Contaminants in Simulated
Wastewater via Tandem Photo-Fenton-like Reaction and
Nutrient Recovery**

| | |
|---------------|---|
| Journal: | <i>Environmental Science: Water Research & Technology</i> |
| Manuscript ID | EW-ART-03-2022-000209.R2 |
| Article Type: | Paper |
| | |

SCHOLARONE™
Manuscripts

Water Impact

Emerging contaminants (ECs) pose a significant risk to the environment when they are incorporated into struvite recovered from nutrient-rich wastewater that contains such hazardous materials. By adding a heterogeneous Fenton oxidation pretreatment step, the ECs can be oxidized, and struvite recovery can be conducted without the risk of incorporating toxic contaminants.

Treatment of Emerging Contaminants in Simulated Wastewater *via* Tandem Photo-Fenton-like Reaction and Nutrient Recovery

Manoj Silva,¹ Mohamed Eisa,¹ Dovilė Ragauskaitė,¹ Madison H. McMinn,² Zhenyu Tian,² Clinton Williams,³ Allan Knopf,³ Lihua Zhang,⁴ and Jonas Baltrusaitis^{1,*}

¹Department of Chemical and Biomolecular Engineering, Lehigh University, B336 Iacocca Hall, 111 Research Drive, Bethlehem, PA 18015, USA

²Department of Chemistry and Chemical Biology, Northeastern University, 02115, MA, USA

³USDA-ARS, US Arid Land Agricultural Research Center, 21881 N. Cardon Ln, Maricopa, AZ, 85138, USA

⁴Brookhaven National Laboratory, Center for Functional Nanomaterials, Upton, NY 11973, USA

Abstract

A tandem strategy that recovers NH_4^+ and PO_4^{3-} nutrients from simulated wastewater in a solid form after the Fenton oxidation of emerging organic contaminants was developed. Mesoporous Cu-MgO nanoparticles were used as a photo-Fenton-like catalyst to oxidize paraoxon and tetracycline present in nutrient-rich simulated wastewater to prevent their incorporation into the struvite product. Mesoporous MgO nanoparticles were subsequently used as the Mg-source for the struvite crystallization due to the fast intraparticle diffusion and adsorption kinetics facilitated by their porosity and the high surface area. Without Fenton oxidation, 13% of paraoxon and 37% of tetracycline were incorporated into the struvite, demonstrating the clear need for the removal of hazardous contaminants before struvite synthesis. Both organic contaminants were eliminated using the Fenton oxidation reaction, with some minor non-toxic intermediate products formed. The product formed after the tandem process was shown by XRD and Raman spectroscopy to be struvite free of the emerging organic contaminants.

*Corresponding author: job314@lehigh.edu, phone +1-610-758-6836

Keywords: heterogeneous photo-Fenton; catalysis; struvite recovery; wastewater treatment; nutrient recycling; emerging contaminants

28 **1 Introduction**

29 The use of modern mineral nitrogen and phosphorus fertilizers has led to an unprecedented
30 productivity increase in the agriculture sector while also leading to significant perturbation of these
31 nutrient cycles.¹⁻⁴ Nitrogen fixation *via* the Haber-Bosch process is used to produce ammonia,
32 which subsequently is converted to urea, the most widely used nitrogen fertilizer in the world.⁵
33 The inefficiency of urea use has been a topic of perennial importance provided that up to 90% of
34 the applied nitrogen can be lost to leaching as runoff, or as greenhouse gas emissions.⁶ The energy
35 cost of nitrogen fixation is estimated to be 1–2% of the global energy consumption and 3–5% of
36 the total natural gas output.⁷ This energy loss caused by the inefficient utilization of fertilizer
37 materials is an important sustainability concern.⁸ In particular, the loss of nitrogen from urea as
38 reactive nitrogen ($\text{N}_2\text{O}_{(\text{g})}$, $\text{NH}_3_{(\text{g})}$, $\text{NO}_2^-_{(\text{aq})}$, $\text{NH}_4^+_{(\text{aq})}$) in the atmosphere and aquatic environment
39 leads to adverse consequences such as climate change and algal blooms.⁹ Similarly, phosphorous
40 discharge in runoff has been identified as a significant driver of eutrophication resulting in aquatic
41 life damage and significant methane emissions.^{9,10} Provided that phosphorous is mined in a limited
42 number of locations worldwide, the geopolitical implications of its future production are of
43 concern.¹¹ Various wastewater streams of anthropogenic origin contain recoverable NH_4^+ and
44 PO_4^{3-} with concentrations up to 1,000 and 1,500 mg/L, respectively.¹² Capturing these nutrients
45 from wastewater in the form of struvite ($\text{MgNH}_4\text{PO}_4 \cdot 6\text{H}_2\text{O}$), a slow-release fertilizer, has been
46 identified as a viable method toward a circular nutrient economy that would alleviate negative
47 environmental impacts of mineral fertilizers.¹³⁻¹⁶ Struvite is synthesized by adding an Mg^{2+} source
48 to NH_4^+ and PO_4^{3-} containing wastewater, with many studies focusing on the use of magnesium
49 chloride. Recent studies showed that insoluble Mg-minerals such as MgO^{17-20} , MgCO_3^{21} ,

50 $\text{CaMg}(\text{CO}_3)_2$ ²²⁻²⁴ can also be used for struvite recovery as potentially more abundant and more
51 sustainable sources, with PO_4^{3-} removal up to 94%.

52 The increasing presence of emerging contaminants (ECs) in wastewater poses a direct challenge
53 for nutrient recovery due to the possible contamination of recovered solid fertilizer materials
54 produced from wastewater-bearing pollutants such as pharmaceuticals, flame retardants,
55 insecticides, herbicides and defoamers.²⁵ Such organic contaminants have been shown to affect
56 the struvite crystallization process including crystal size and morphology.^{26,27} An example has
57 been reported where producing struvite from wastewater with the antibiotic tetracycline (TCL)
58 present was shown to lead to its adsorption on the resulting struvite crystals.²⁸ Use of such
59 contaminated struvite can lead to the alteration of the antibiotic resistome of soil and the
60 rhizosphere.^{29,30} Similarly, organophosphates are another increasingly common class of ECs that
61 have detrimental effects on human health due to their environmental accumulation in soil, plants,
62 and animal tissues.³¹⁻³⁴ Paraoxon-ethyl (p-OXN) has been reported to be a metabolite of parathion-
63 ethyl, an organophosphate compound that is used as an insecticide.^{35,36} Parathion is readily
64 converted to paraoxon in the presence of sunlight.³⁷ The cholinesterase inhibition action of p-
65 OXN renders it toxic to humans, while reports also show that exposure to even low doses of p-
66 OXN can induce transgenerational effects.^{36,38} Soil is a natural reservoir of both antibiotics and
67 antibiotic-resistance genes, and as such, the addition of further antibiotic-containing compounds
68 has severe consequences on the soil as well as crops grown in the contaminated soil.³⁹ The toxicity
69 of ECs makes them recalcitrant toward traditional biological treatment and thus, they require
70 harsher chemical oxidation treatments.⁴⁰ Advanced oxidation processes (AOPs) have emerged as
71 a viable method of treating ECs, as the radicals produced during AOPs are powerful oxidizers
72 capable of remediating toxic contaminants without hindrance.⁴¹⁻⁴³

73 This study is focused on investigating a tandem process whereby the first stage utilizes the photo-
74 Fenton-like reaction to degrade the ECs using Cu doped MgO nanoparticles (NPs) while in the
75 second stage mesoporous MgO particles are used to synthesized struvite. First, equilibrium
76 modeling was used to determine the Cu-MgO catalyst loading that would lead to high activity
77 while avoiding struvite nucleation on the MgO support by using undersaturated conditions and to
78 determine the optimal MgO loading used to recover struvite following the Fenton oxidation stages
79 and catalyst removal. Next, EC incorporation in struvite was investigated without the Fenton
80 oxidation step to confirm that TCL and p-OXN can contaminate the product struvite when nutrient
81 recovery is conducted in the presence of ECs. Finally, the tandem process was tested with Stage 1
82 as the Fenton oxidation stage, followed by catalyst separation and Stage 2, where nutrient recovery
83 with undoped MgO was conducted. The use of an AOP conducted at a neutral to alkaline pH
84 environment ensured EC decomposition on the active copper metal center without leaching the
85 metal into the aqueous phase. A semi-continuous injection of H_2O_2 was used to minimize the
86 production of larger intermediate molecules as suggested in previous work.^{44,45}

87 **2 Materials and Methods**

88 **2.1 Mesoporous Cu-MgO and undoped MgO nanoparticle synthesis**

89 A facile thermal decomposition procedure was modified and used to synthesize undoped MgO
90 NPs and 5% (by weight) Cu-MgO [22,30]. Briefly, a solution of $Mg(NO_3)_2 \cdot 6H_2O$
91 (MilliporeSigma, 99%) and $Cu(NO_3)_2 \cdot 3H_2O$ (Sigma, 99+%) was prepared in methanol with the
92 required mass ratios and a 0.59 M NaOH/methanol solution was added dropwise under reflux
93 temperature. For the preparation of undoped MgO, $Cu(NO_3)_2 \cdot 2H_2O$ was omitted while keeping
94 the same procedure. After 30 minutes of reaction at reflux temperature, the resulting precipitate
95 was collected by centrifugation, washed three times using a 1:1 ratio of ethanol/water solution and

96 dried at 80 °C overnight. The dry solid was calcined at 450 °C for 2 hours (2 °C/min ramp rate) in
97 static air. Next, 0.5 g of the prepared material was added to 40 ml deionized water and stirred for
98 12 hours. After stirring, the gel was separated by centrifugation and dried at 80 °C. The sample
99 was then calcined at 450 °C for 2 hours (2 °C/min ramp rate) in static air to obtain the final catalyst.

100 **2.2 Photocatalytic degradation experiments**

101 The p-OXN and TCL solutions were prepared by dissolving p-OXN (Acros Organics, 99+%) and
102 TCL (Alfa Aesar, 91+%) in deionized water (Millipore). The concentrations for p-OXN and TCL
103 were chosen to be 25 mg/L, consistent with previous literature reports discussing their presence in
104 wastewater streams.^{46,47} The catalyst concentration used was 250 mg/L (as discussed in **Section**
105 **3.1**). A glass vessel containing 100 mL volume of EC solution was used in all experiments. In all
106 experiments, an initial 20 mM dose of H₂O₂ was injected, followed by an additional 5 mM dose at
107 15-minute intervals. The vessel was irradiated by a 350 W xenon lamp (Newport), which provided
108 an illumination intensity of approximately 100 mW cm⁻². 1 mL of solution was periodically
109 filtered with a 0.22 µm membrane and measured HPLC to quantify EC concentration.

110 *Ion Chromatography (IC)*. The Metrohm Eco 925 IC system (Herisau, Switzerland) was used to
111 measure the ion composition of the reacted solutions. Separation columns used were Metrosep A
112 supp 4/5 Guard column (5 × 4 mm), Metrosep A supp 5 (4 × 150 mm) for anion analysis and
113 Metrosep C 4 Guard column (5 × 4 mm), Metrosep C 4 (4 × 150 mm) for cation analysis. The
114 sample-loop volume was 10 µL in the cation system and 20 µL in the anion system, and eluted
115 species were measured using a conductivity detector. Dipicolinic acid (1.75 nM HNO₃/0.7 mM)
116 was used as an eluent for Metrosep C 4 while 3.2 mM Na₂CO₃/1.0 mM NaHCO₃ for Metrosep A
117 supp 5. All samples were measured at room temperature. The system was controlled through
118 MagIC Net 3.2 software.

119 *High Resolution Mass Spectrometry (HRMS)*. High resolution mass spectral analysis was
120 performed on a Exploris 240 HESI-q-Orbitrap mass spectrometer (ThermoFisher Scientific).
121 Samples were injected using a syringe pump at a rate of 5 $\mu\text{L}/\text{min}$ to a T junction, where it met a
122 solvent composition of 50% Methanol with 0.1% Formic acid / 50% Water with 0.1% Formic acid
123 (positive ion mode) or 50% Methanol / 50% 1 mM Ammonium Fluoride (negative ion mode)
124 flowing at a rate of 0.1 mL/min from a Vanquish HPLC system (ThermoFisher Scientific) for
125 tetracycline samples. For p-OXN, analysis was performed using the same conditions, but a mobile
126 phase composition of 100% Water with 0.1% Formic acid (positive ion mode) or 100% 1 mM
127 Ammonium Fluoride (negative ion mode).

128 Positive ion mode data was acquired using the following HESI source settings: spray voltage =
129 3,500 V, sheath gas (Arb) = 50, aux gas (Arb) = 5, sweep gas (Arb) = 0, ion transfer tube
130 temperature = 320 $^{\circ}\text{C}$, and vaporizer temperature = 300 $^{\circ}\text{C}$. For full scan (MS^1 , the following
131 mass spectral settings were used: Orbitrap Resolution (FWHM, at m/z 200) = 120,000, scan range
132 = m/z 50 – 750, RF lens % = 60, AGC target = 100, source fragmentation = OFF. For fragmentation
133 (MS^2) (Tetracycline precursor ion = $[\text{M}+\text{H}]^+ = m/z$ 445.1610; p-OXN precursor ion = $[\text{M}+\text{H}]^+ =$
134 m/z 276.0632) the following mass spectral settings were used: isolation width = 0.4 m/z , HCD
135 collision energy (absolute) = 17 V, all other settings were the same as full scan mode.

136 Negative ion mode data was acquired using the following HESI source settings: spray voltage =
137 3,200 V, sheath gas (Arb) = 50, aux gas (Arb) = 5, sweep gas (Arb) = 0, ion transfer tube
138 temperature = 320 $^{\circ}\text{C}$, and vaporizer temperature = 300 $^{\circ}\text{C}$. For full scan (MS^1 , the following
139 mass spectral settings were used: Orbitrap Resolution = 120,000, scan range = m/z 50 – 750, RF
140 lens % = 120, AGC target = 100, source fragmentation = OFF. . For fragmentation (MS^2) of
141 (Tetracycline precursor ion = $[\text{M}-\text{H}]^- = m/z$ 443.1461; p-OXN precursor ion = $[\text{M}-\text{H}]^- = m/z$

142 274.0486) the following mass spectral settings were used: isolation width = 0.4 m/z , HCD collision
143 energy (absolute) = 17 V, all other settings were the same as full scan mode.

144 Data was analyzed and figures were created in FreeStyle 1.8 SP2 (ThermoFisher Scientific). Mass
145 spectral matching for tetracycline was done using m/z Cloud (ThermoFisher Scientific).

146 **2.3 Struvite synthesis.** Simulated NH_4^+ and PO_4^{3-} containing wastewater samples were prepared
147 by adding 1500 mg/L of monoammonium phosphate (MAP), $\text{NH}_4\text{H}_2\text{PO}_4$ (99.9 %+, Fisher
148 Scientific) in 18.2 M Ω /cm deionized water (Millipore, USA). A 1500 mg/L MAP solution
149 represents PO_4^{3-} and NH_4^+ values found in municipal, animal and industrial wastewater¹² while
150 maintaining above the molar 1:1 ratio needed for struvite formation. MgO NPs were added to 500
151 mL of the simulated wastewater and stirred for up to 120 minutes. Aliquots of 0.5 mL were
152 sampled periodically, filtered through a 0.22 μm polyethersulfone filter, and analyzed using ion
153 chromatography. The MgO concentration used for struvite synthesis was 750 mg/L, which
154 corresponds to molar $[\text{Mg}^{2+}]:[\text{NH}_4^+]:[\text{PO}_4^{3-}]$ ratio of 1.44:1:1. $[\text{Mg}^{2+}]:[\text{NH}_4^+]:[\text{PO}_4^{3-}]$ ratios of 0.5-
155 1.5:1:1 have previously been tested and was concluded that lower ratios lead to a lesser N and P
156 adsorption/reaction.^{18,48,49} Therefore, a slight excess of Mg^{2+} was preferred in the previous works
157 to circumvent this issue and ensure efficient removal of N and P from the solution.^{50,51} The kinetics
158 of adsorption were analyzed using the pseudo-second order equation (Equation 1).⁵²

159
$$t/q_t = 1/k_2q_e^2 + t/q_e \quad (1)$$

160 The pseudo-second order rate constant is denoted by k_2 ($\text{g}_{\text{MgO}}\text{mg}_{\text{PO}_4}^{-1}\text{min}^{-1}$), the adsorbed PO_4
161 concentration at time t (min) is denoted by q_t ($\text{mg}_{\text{PO}_4}\text{g}_{\text{MgO}}^{-1}$), and the adsorbed PO_4 concentration
162 at equilibrium is denoted by q_e ($\text{mg}_{\text{PO}_4}\text{g}_{\text{MgO}}^{-1}$).

163 For struvite synthesized in the presence of ECs, a solution containing 25 mg/L of the EC (either
164 TCL or p-OXN) and 1500 mg/L MAP was prepared. To this solution, 750 mg/L of MgO NPs were
165 added to produce struvite. For the tandem process (shown in Figure 1), the Cu-MgO catalyst used
166 in the oxidation step was first removed *via* filtration, and following catalyst removal, 750 mg/L of
167 MgO NPs were added to the solution to initiate struvite formation.

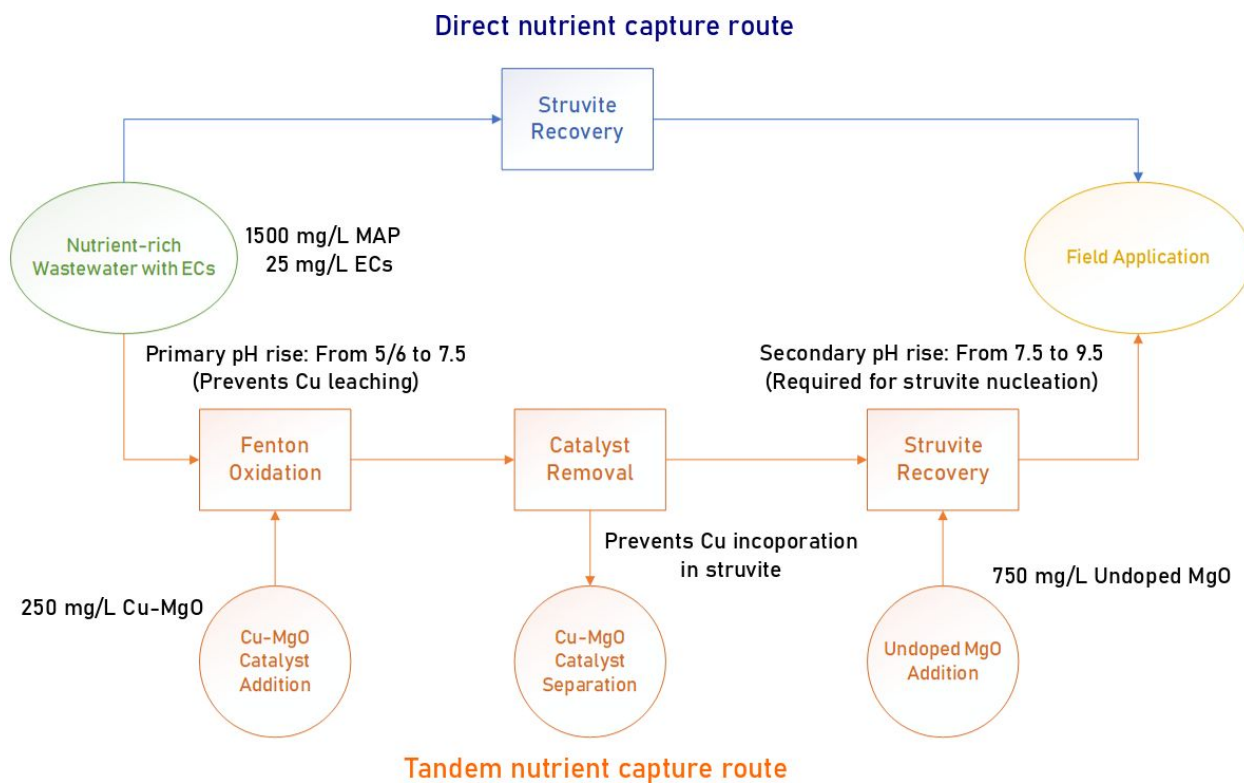
168 *Saturation Index (SI) Calculations.* Visual Minteq 3.1 software was used to calculate SI values of
169 the potential solid products at equilibrium.⁵³ The pH in each case was varied over the range
170 measured during each experiment. The ionic strength was not fixed but rather calculated from the
171 ion balance. Concentrations of 250 mg/L of NH_4^+ and 1250 mg/L PO_4^{3-} were held constant in all
172 calculations while the Mg^{2+} ion concentration was set to that of the Mg from the initial MgO and
173 the Mg^{2+} measured from the aqueous phase to study phosphate adsorption and homogeneous
174 nucleation. A temperature of 25 °C was used to mimic experimental conditions.

175 **2.4 Struvite physicochemical characterization**

176 *Powder X-ray Diffraction.* The crystal structure of all catalysts was confirmed using powder X-
177 ray diffraction (Empyrean, PANalytical B.V.). The applied current was 40 mA and the applied
178 voltage was 45 kV. The X-ray mirror that was used was a graded, flat Bragg-Brentano HD mirror,
179 with the step size set to 0.0131 degrees.

180 *Raman spectroscopy.* Horiba-Jobin Yvon LabRam HR (high-resolution) spectrometer equipped
181 with a 442 nm laser. The laser was focused through a confocal microscope with a 50× objective
182 (Olympus BX-30-LWD). Before spectra were collected, the Raman spectrometer was calibrated
183 with a silicon standard possessing a reference band at 520.7 cm^{-1} . The spectral resolution of the
184 spectrometer is $\sim 1 \text{ cm}^{-1}$, and the spectra were collected with 600 grating, 5 scans (30 s/scan) and
185 a 100 μm pinhole.

186 *Scanning electron microscopy*. All SEM images were obtained using a Hitachi 4300 SE FE-SEM.
 187 A 5.0 kV voltage setting was used with an aperture setting of 3 and a gun brightness of 1.



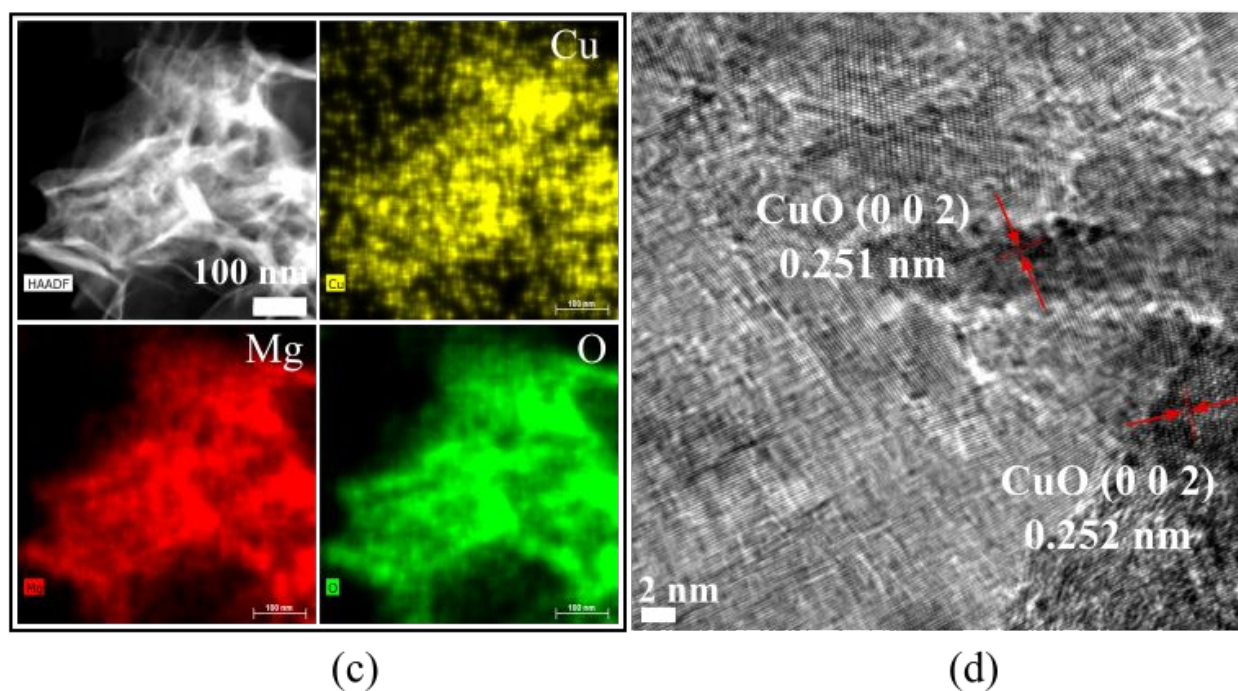
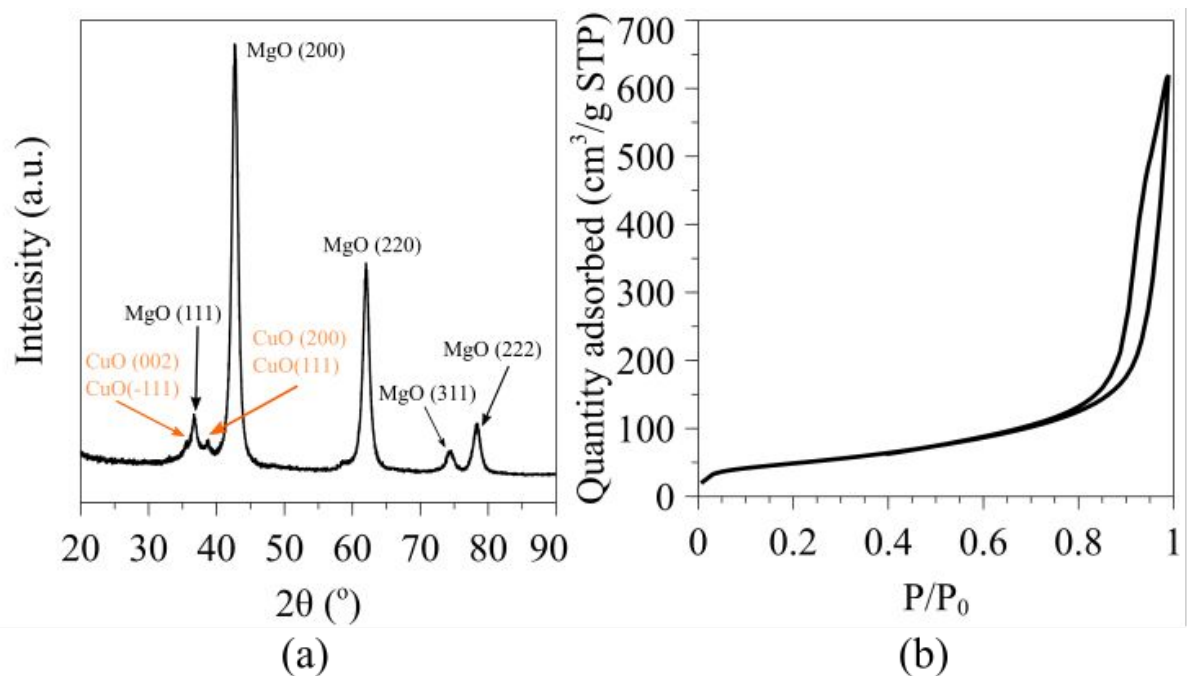
188
 189 Figure 1. Graphical representation of the tandem photo-Fenton-like oxidation and subsequent
 190 nutrient recovery process studied in this work.

191 3 Results and Discussion

192 3.1 Physicochemical characterization of Cu-MgO NPs

193 The photo-Fenton-like oxidation of the selected ECs using mesoporous Cu-MgO NPs was
 194 proposed recently.⁴⁵ The use of such basic solid catalysts that operate in neutral to alkaline
 195 environments has been demonstrated to lead to catalyst operation free of metal leaching in the
 196 aqueous phase.^{45,54,55} Figure 2 shows a summary of the physicochemical characterization of as-
 197 synthesized Cu-MgO with emphasis on the crystal structure and pore textural properties. As shown
 198 in Figure 2(a), the XRD pattern for the 5% Cu-MgO contains all the major peaks corresponding to

199 MgO, while several minor peaks are present matching those of CuO. Specifically, the region
200 between 2θ angles $30^\circ - 40^\circ$ displayed peaks corresponding to (0 0 2), (-1 1 1), (2 0 0), and (1 1
201 1) of CuO in addition to MgO peaks.⁵⁶⁻⁵⁸ Cu and Mg have similar ionic radii (73 and 72 Å,
202 respectively) and this causes both the solid solution of MgO and CuO as well as a separate CuO
203 nanoparticle phase to form in this catalyst.^{56,57} The mesoporous structure of the catalyst material
204 is evident from the Type IV isotherm observed by nitrogen physisorption shown in Figure 2(b).
205 The surface area for the Cu-MgO NPs was measured to be $170 \text{ m}^2/\text{g}$ with $0.974 \text{ cm}^3/\text{g}$ pore volume.
206 The high surface area and porosity facilitate faster intraparticle diffusion, leading to faster reaction
207 kinetics.⁵⁴ Figures 2(c) and (d) show HAADF STEM-EDS and HR-TEM images for the Cu-MgO
208 nanoparticles. Cu dispersion over the MgO is evident in HAADF-STEM-EDS, while the HR-TEM
209 allowed for d-spacing to be measured, confirming the presence of CuO nanoparticles dispersed
210 over the MgO support. The CuO (0 0 2) d-spacing was measured to be between 0.251-0.252 nm.⁵⁹
211 Previous work on Cu-MgO NPs utilized XANES to confirm that CuO was present in the as-
212 synthesized catalysts and that CuO was the sole phase of Cu in the as-synthesized catalysts.²⁰



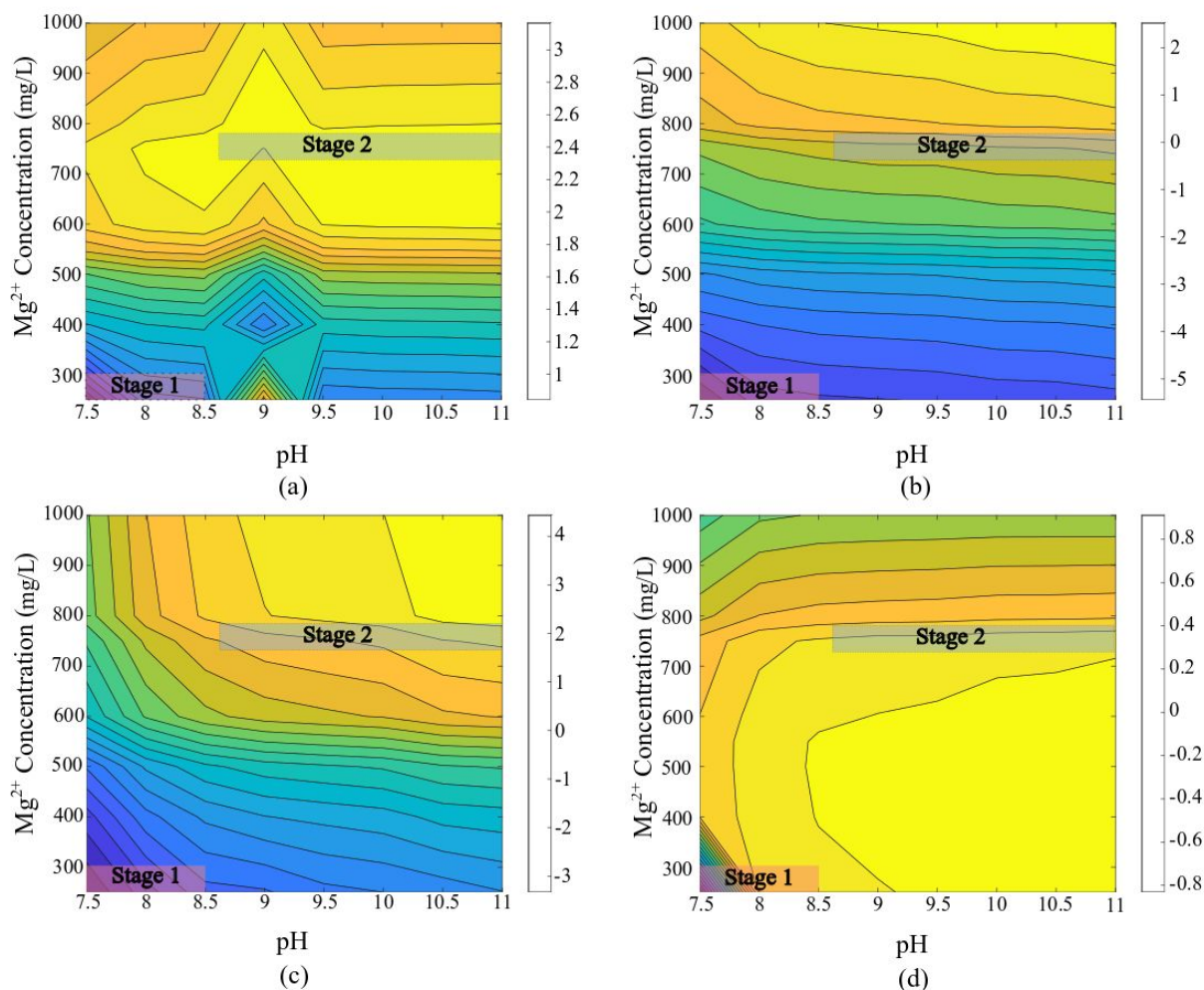
213

214 Figure 2. Cu-MgO characterization (a) XRD pattern (b) Nitrogen physisorption isotherm (c)

215 STEM-EDS Maps (d) HR-TEM image for 5% Cu-MgO

216 **3.2 Equilibrium-based modeling of precipitate phase speciation**

217 The precipitation of struvite and other magnesium phosphate phases is determined by a
218 combination of the pH of the solution, as well as the activity of the ion species that comprise the
219 various possible precipitates. While struvite is the desired product of the nutrient recovery process,
220 various magnesium phosphate phases such as $\text{MgHPO}_4 \cdot 3\text{H}_2\text{O}$ and $\text{Mg}_3(\text{PO}_4)_2 \cdot 22\text{H}_2\text{O}$ and the
221 hydroxide phase brucite ($\text{Mg}(\text{OH})_2$) can also precipitate depending on the thermodynamic
222 favorability of formation.¹⁸ The most useful thermodynamic parameter that can model the
223 equilibrium distribution of precipitates as a function of pH and ion activity is the SI.^{60,61} Visual
224 Minteq was used to model the SI as a function of pH and Mg^{2+} ion concentration in the solution to
225 guide the experimental design. In equilibrium simulations of struvite recovery, it was assumed that
226 nearly all of the Mg^{2+} is available due to enhanced transport rates facilitated by the higher surface
227 area and more efficient intraparticle diffusion in mesoporous MgO.



228
 229 Figure 3. SI for (a) struvite (b) brucite (c) $\text{Mg}_3\text{PO}_4 \cdot 22\text{H}_2\text{O}$ (d) $\text{MgHPO}_4 \cdot 3\text{H}_2\text{O}$ as a function of pH
 230 and Mg^{2+} concentration in the aqueous phase (SI shown by the color bar).

231 Figure 3 shows the saturation indices as a function of pH and Mg^{2+} concentration for struvite,
 232 $\text{Mg}(\text{OH})_2$, $\text{Mg}_3\text{PO}_4 \cdot 22\text{H}_2\text{O}$, and $\text{MgHPO}_4 \cdot 3\text{H}_2\text{O}$. Indeed, the solution pH remains under 7.5 when
 233 the Cu-MgO concentration is <300 mg/L, which results in saturation indices being near zero or
 234 negative (highlighted area for Stage 1 in Figure 3). This agrees with previous work where the
 235 0.44:1:1 ratio of $\text{Mg}^{2+}:\text{NH}_4^+:\text{PO}_4^{3-}$ not producing struvite (or other precipitates).¹⁸ This
 236 undersaturated condition is desired since the NH_4^+ and PO_4^{3-} are not expected to adsorb on the

237 catalyst, which allows the Fenton oxidation to proceed without perturbing the nutrients in the
238 solution.

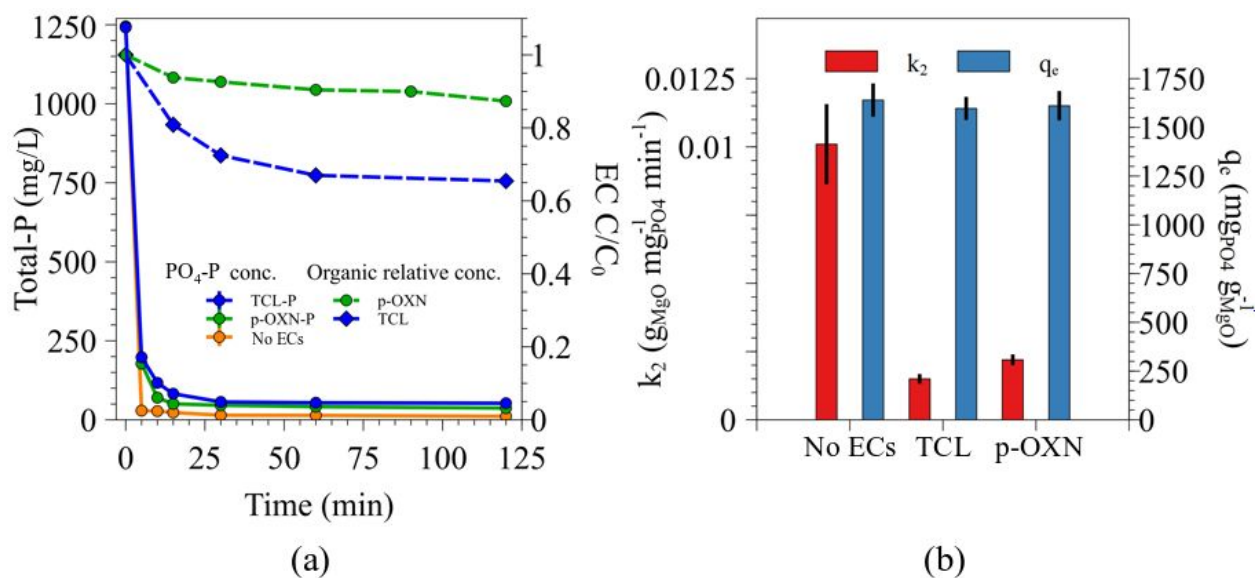
239 A $\text{Mg}^{2+}:\text{NH}_4^+:\text{PO}_4^{3-}$ the ratio of 1.44:1:1 is the optimal ratio for struvite synthesis from MgO with
240 no detectable magnesium phosphate by-product formation with no external pH control as reported
241 previously on both microcrystalline and nanostructure MgO.^{18,20} Higher ratios (such as 4.8:1:1)
242 were shown to produce magnesium phosphate phases that did not contain NH_4^+ .^{18,20} This behavior
243 has been reported for other insoluble Mg-sources such as dolomite ($\text{CaMg}(\text{CO}_3)_2$)²² and magnesite
244 (MgCO_3).²¹ the pH value is desired to be in the 7.5 – 10 range for struvite crystallization. Following
245 catalyst separation, undoped MgO is added as the Mg-source for struvite recovery. This addition
246 of MgO leads to the rapid rise of pH above 9, which causes the SI for struvite and $\text{Mg}_3\text{PO}_4 \cdot 22\text{H}_2\text{O}$
247 become higher than 1, indicating supersaturation. For the MgO concentration of ~750 mg/L, the
248 saturation indices for $\text{Mg}(\text{OH})_2$ and $\text{MgHPO}_4 \cdot 3\text{H}_2\text{O}$ show that these phases are not
249 thermodynamically favored to be major products, as their saturation indices are significantly lower
250 than struvite or $\text{Mg}_3\text{PO}_4 \cdot 22\text{H}_2\text{O}$. Between struvite and $\text{Mg}_3\text{PO}_4 \cdot 22\text{H}_2\text{O}$, it can be seen that the
251 saturation indices vary between 2.8 and 3.3 and that the struvite SI is slightly higher in the 7.5 –
252 9.5 pH range at 750 mg/L of MgO loading. As the pH increases beyond 10 and higher MgO
253 loadings (up to 1,000 mg/L) are present, the $\text{Mg}_3\text{PO}_4 \cdot 22\text{H}_2\text{O}$ SI value increases beyond that of
254 struvite, indicating that the dominant phase at higher pH values and higher MgO loadings would
255 be $\text{Mg}_3\text{PO}_4 \cdot 22\text{H}_2\text{O}$. This is consistent with previous studies reporting PO_4^{3-} adsorption kinetics
256 over a larger range of MgO loadings and pH values.^{18,20,21} Therefore, pH control and MgO loading
257 selection become important considerations in the process design of struvite recovery, as these two
258 parameters can determine the product speciation. While the struvite SI is only slightly higher than
259 the SI for $\text{Mg}_3\text{PO}_4 \cdot 22\text{H}_2\text{O}$ during this stage, it is important to consider that Visual Minteq models

260 the thermodynamic products, without considering kinetic products. Therefore, in the critical region
261 of struvite growth (the initial 10 minutes where the rapid pH rises from 7.5 to 9.5 occurs), struvite
262 is most likely to be kinetically favored to precipitate, even though $\text{Mg}_3\text{PO}_4 \cdot 22\text{H}_2\text{O}$ is also
263 thermodynamically favored to precipitate, but is not found to be a major product kinetically.¹⁸

264 **3.3 Effects of ECs on struvite production during direct nutrient capture route**

265 Before studying the tandem process of Fenton oxidation and struvite recovery, the effect of ECs
266 on struvite crystallization was studied separately to understand how EC incorporation occurs in
267 the absence of Fenton oxidation before struvite crystallization (the direct nutrient capture route
268 presented in Figure 1). In this study, simulated wastewater consisting of 1500 mg/L MAP and 25
269 mg/L of ECs was used to produce struvite using undoped MgO as the Mg-source. Struvite
270 crystallization was initiated by adding 750 mg/L of MgO NPs to a 1500 mg/L MAP solution in
271 the dark. The experiment was conducted in the dark to avoid light-induced reactions involving the
272 ECs.⁵⁴ The 750 mg/L MgO loading was used as this was expected to reach the desired SI value
273 consistent with the highlighted Stage 2 region in Figure 3(a). Figure 4(a) shows the relative
274 concentrations of the ECs during struvite synthesis with simultaneously measured Total-P
275 concentration for three experiments: no ECs present, TCL, and p-OXN. The p-OXN and TCL
276 show 13% and 37% relative concentration reduction over a 2-hour reaction time, demonstrating
277 that both contaminants can be incorporated into the product struvite. Therefore, the need for a
278 pretreatment step of oxidizing the ECs before struvite formation becomes critical, as struvite
279 contaminated with ECs leads to significant environmental hazards.^{28,29} In all three cases (no ECs,
280 p-OXN, and TCL), the PO_4^{3-} removal remains high, with 99%, 97%, and 95%, respectively. Figure
281 4(b) shows the pseudo-second order kinetic analysis results for the three cases of forming struvite:
282 namely without ECs and the two scenarios with TCL and p-OXN. The adsorbed phosphate

283 concentrations from the initial 30 minutes of the reaction were fitted to the pseudo-second order
284 equation as the reaction approaches equilibrium within the first 30 minutes. The pseudo-second
285 order equation was used since previous work on MgO has shown that the data with a higher quality
286 of fit compared to the pseudo-first order, and since the pseudo-first order equation is more
287 applicable to systems where the bulk adsorbate concentration does not vary significantly.^{10,18,62}
288 The phosphate concentrations during the first 30 minutes of reaction were fitted to the pseudo-
289 second order equation to calculate the rate constant and phosphate adsorbed at equilibrium. Since
290 phosphate adsorption on mesoporous MgO rapidly approaches equilibrium, with the majority of
291 the phosphate adsorbed within the first 10 minutes, fitting to the first 30 minutes becomes
292 sufficient.²⁰ The k_2 values for the no ECs present, TCL, and p-OXN experiments were calculated
293 to be $0.01 \text{ g mg}^{-1} \text{ min}^{-1}$, $0.0015 \text{ g mg}^{-1} \text{ min}^{-1}$, $0.0022 \text{ g mg}^{-1} \text{ min}^{-1}$, respectively. The concentration
294 of phosphate adsorbed at equilibrium or q_e values were calculated to be $1,640 \text{ mg g}^{-1}$, $1,597 \text{ mg}$
295 g^{-1} , and $1,611 \text{ mg g}^{-1}$, respectively. The first 30 minutes of phosphate adsorption show a kinetic
296 hindrance when ECs are present, but the equilibrium phosphate removal achieved after 2 hours of
297 reaction does not show a large variation. However, the EC incorporation when struvite is formed
298 in the presence of TCL and p-OXN shows the need for the photo-Fenton-like oxidation stage.



299 (a) (b)

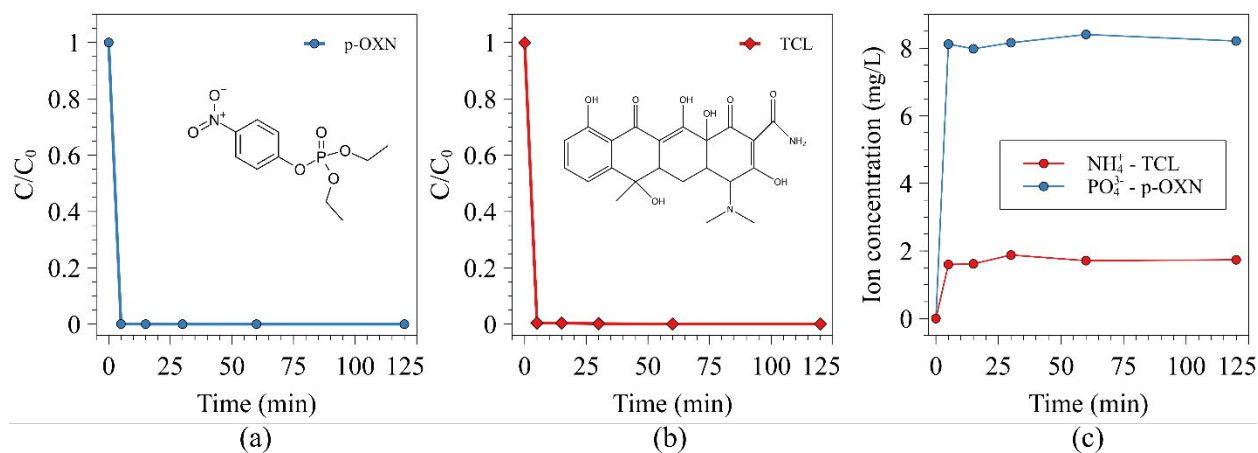
300 Figure 4. (a) EC relative concentrations (dashed lines) and Total-P concentration (solid lines) over
 301 time during struvite synthesis in the presence of ECs (b) Pseudo-second order rate constant and
 302 equilibrium adsorbed PO_4^{3-} concentration for control and in the presence of ECs.

303 3.4 Photo-Fenton-like catalysis of ECs using Cu-MgO NPs

304 The propensity of Cu-MgO particles to oxidize the two ECs of interest was first established. The
 305 Cu-MgO catalyst concentration was chosen to be 250 mg/L for the photo-Fenton-like oxidation
 306 reaction of ECs based on the SI calculations, as 250 mg/L Cu-MgO does not lead to any
 307 precipitation of struvite due to the undersaturated conditions as discussed in **Section 3.2**. The
 308 photo-Fenton-like oxidation was first studied in the absence of MAP in the solution. Figure 5(a)
 309 and 5(b) show the relative concentrations of p-OXN and TCL, respectively (C/C_0 where C denotes
 310 the concentration at time t , and C_0 denotes the initial concentration of 25 mg/L). The parent
 311 structures of the ECs are broken down completely within the first 5 minutes of reaction, as both
 312 species show a rapid decrease by the 5-minute time point. The overall reaction time for both ECs
 313 was 2 hours due to prior literature on TCL, and in the case of p-OXN, the MS spectra showed no

314 change past 2 hours of reaction (further discussed in **Section 3.5**). The measured p-OXN and TCL
 315 concentrations after 120 minutes of reactions were 0.00 mg/L and 0.02 mg/L, respectively, which
 316 corresponds to over 99% conversion in both cases.

317 Further, to understand the fate of the heteroatoms N and P in TCL and p-OXN, experiments were
 318 conducted where 25 mg/L of TCL and p-OXN were reacted with 250 mg/L Cu-MgO and IC were
 319 used to measure the concentration of NH_4^+ and PO_4^{3-} over the reaction time. Figure 5(c) shows the
 320 inorganic ion concentrations for these two experiments. Importantly, within the first 5 minutes of
 321 reaction, the NH_4^+ and PO_4^{3-} resulting from heteroatoms in each respective EC reached the
 322 stoichiometric value expected if all of the N and P were converted to NH_4^+ and PO_4^{3-} , respectively.
 323 These ions can also be recovered with the nutrients already present in their ionic form in
 324 wastewater.



325
 326 Figure 5. The relative concentration of ECs as a function of the reaction time under the photo-
 327 Fenton-like reaction phase for (a) p-OXN (b) TCL. (c) Inorganic ions (the N and P in TCL and p-
 328 OXN, respectively), are liberated during the reaction and measured as NH_4^+ and PO_4^{3-} using IC.

329 3.5 Semi-continuous H_2O_2 delivery for photo-Fenton-like oxidation

330 As discussed in the section above, the Cu-MgO catalyst led to the complete oxidation of the parent
331 structures of TCL and p-OXN, and the liberation of the heteroatoms as NH_4^+ and PO_4^{3-} for TCL
332 and p-OXN, respectively. While the parent structures were eliminated, various smaller
333 intermediate species can be present in the solution. Previous work on using the heterogeneous
334 Fenton reaction to remediate ECs has shown that to minimize the amount of intermediate a semi-
335 continuous H_2O_2 delivery should be used instead of a single dose, as this ensures a constant
336 presence of H_2O_2 in the solution that can be activated to produce radicals.^{44,45} As the number of
337 intermediates are reduced to smaller molecules, the toxicity of the solution compared to the parent
338 molecules has been shown to dramatically decrease, and achieve non-toxicity.^{46,63} A previous
339 study using the Cu-MgO and a single dose of H_2O_2 at the beginning of the reaction revealed that
340 a larger distribution of products would be present after the reaction due to inefficient utilization of
341 H_2O_2 .⁴⁵ Therefore, the Fenton reaction in this study utilizes this semi-continuous H_2O_2 delivery,
342 and time-resolved mass spectrometry was used to monitor the intermediates in the solution.

343 As shown in Figure 6, High-Resolution Mass Spectrometry (HRMS) was used to investigate the
344 degradation of TCL and p-OXN in MAP at different timepoints of the Fenton oxidation (0, 15, 60
345 and 120 minutes). p-OXN and TCL were detected in the 0 min solution in both positive and
346 negative ion mode, however detection of p-OXN and TCL in addition to any resulting degradation
347 products was limited in negative ion mode and will not be discussed in detail. TCL in both positive
348 and negative ion mode was shown to be fully degraded within 15 minutes (Figure 6a). With the
349 degradation of TCL, there is an emergence of low m/z species in the 15, 60, and 120 minute
350 samples. However, upon further investigation the majority of these ions can be traced back to MAP
351 and the MgO catalyst (Figure 6b). Identification of degradation products was challenging by
352 HRMS due to the presence of ammonium and phosphate ions from the MAP, which may be

353 contributing to ion suppression and masking the presence of any TCL degradation products.
354 Analysis was further complicated by the presence of with Mg^{2+} ions from the MgO catalyst,
355 resulting in the formation of $[\text{M}+\text{Mg}]^+$ adducts in the resulting mass spectra. The presence of Mg
356 adducts was determined based on isotope fine structure, due to the natural abundance of Mg
357 isotopes resulting in a unique M+1 and M+2 pattern. Another reason as to why degradation
358 products are not readily observed is that by the 15 minute mark TCL had undergone complete
359 mineralization into products not detectable by HRMS. Two potential degradation products of TCL
360 were identified in positive ion mode (m/z 185.0057 = $\text{C}_4\text{H}_{10}\text{O}_3\text{P}+\text{Mg}_2$ and m/z 184.9695 =
361 $\text{CH}_6\text{O}_7\text{P}+\text{Mg}$). Similar observations were made for analysis of p-OXN. p-OXN was found to be
362 fully degraded after 15 minutes (Figure 6c). Detection of p-OXN in negative ion mode was limited
363 at all timepoints, and there were no notable degradation products observed. In positive ion mode,
364 while upon initial evaluation there appears to be numerous degradation products, once subjected
365 to MS² it becomes clear that the major peaks are Mg clusters of several very small molecules,
366 suggesting that p-OXN also underwent mineralization.

367 Alternatively, previous work has shown that TCL breaks down into linear acids such as oxalic
368 (m/z = 90), acetic (m/z = 60), and malonic (m/z = 103) acids using heterogeneous Fenton like
369 reactions.⁶⁴ These linear acids do not pose the toxicity risks that are presented by the parent
370 molecules, or some of the larger intermediates reported to be found in other reports.^{46,63}
371 Unambiguous detection of these linear acid products, however, is not possible due to the
372 overlapping peaks due to the catalyst matrix shown in Figure 6b.

373

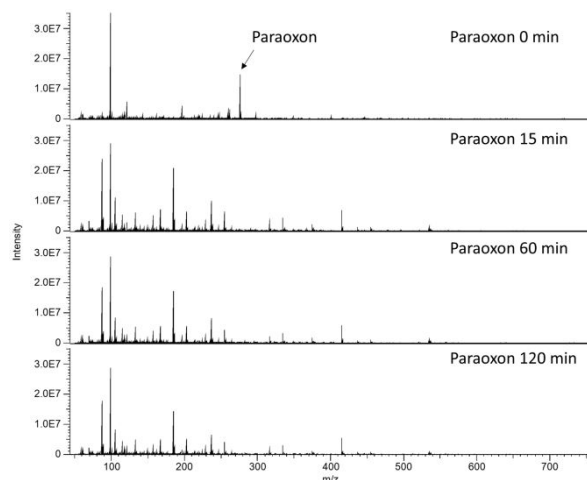
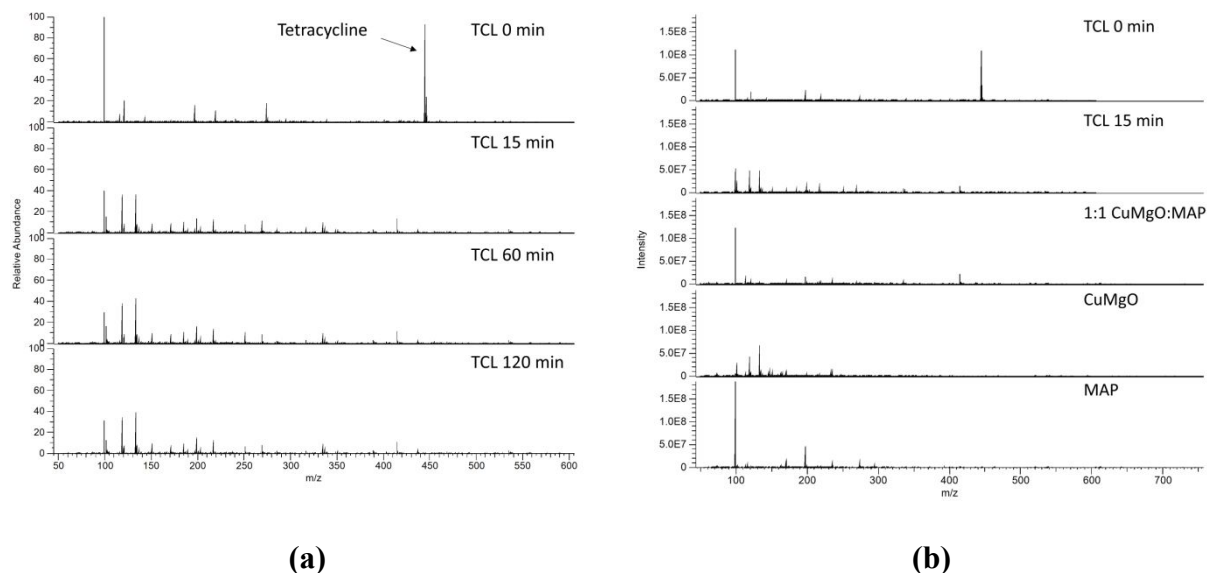


Figure 6. Time-resolved MS spectra for (a) TCL and (b) p-OXN during the photo-Fenton-like oxidation (250 mg/L Cu-MgO catalyst + 25 mg/L EC (p-OXN or TCL) + 20 mM initial H₂O₂ dose followed by 5 mM doses at 15-minute intervals).

374 The oxidation of ECs using oxygen radicals is a multi-step process due to the cleavage of the
375 various C-H, C-C, C-O, C-N bonds, which leads to ECs being broken down into smaller
376 intermediate molecules, before being mineralized to CO₂ and H₂O, along with other inorganic ions
377 that are produced due to the presence of heteroatoms such as N and P. Previous work using Cu-

378 MgO has demonstrated that both $\cdot\text{OH}$ radicals and $\text{HO}_2\cdot/\cdot\text{O}_2^-$ radicals are involved in the
379 degradation of ECs.⁴⁵ TCL has been studied in multiple previous reports, and several of the
380 intermediate molecules have been identified.^{46,63–65} The ROS generated by the catalytic activation
381 of H_2O_2 causes the scission of C-C and C=C bonds, which cause the aromatic rings of TCL and p-
382 OXN to be broken to produce both smaller aromatic products and linear products.⁶⁶ For TCL,
383 previous studies have proposed degradation pathways where the initial 4 benzene rings are cleaved
384 step-wise to produce intermediates containing 1-3 rings, while also removing all N atoms from the
385 TCL parent structure.⁶⁶

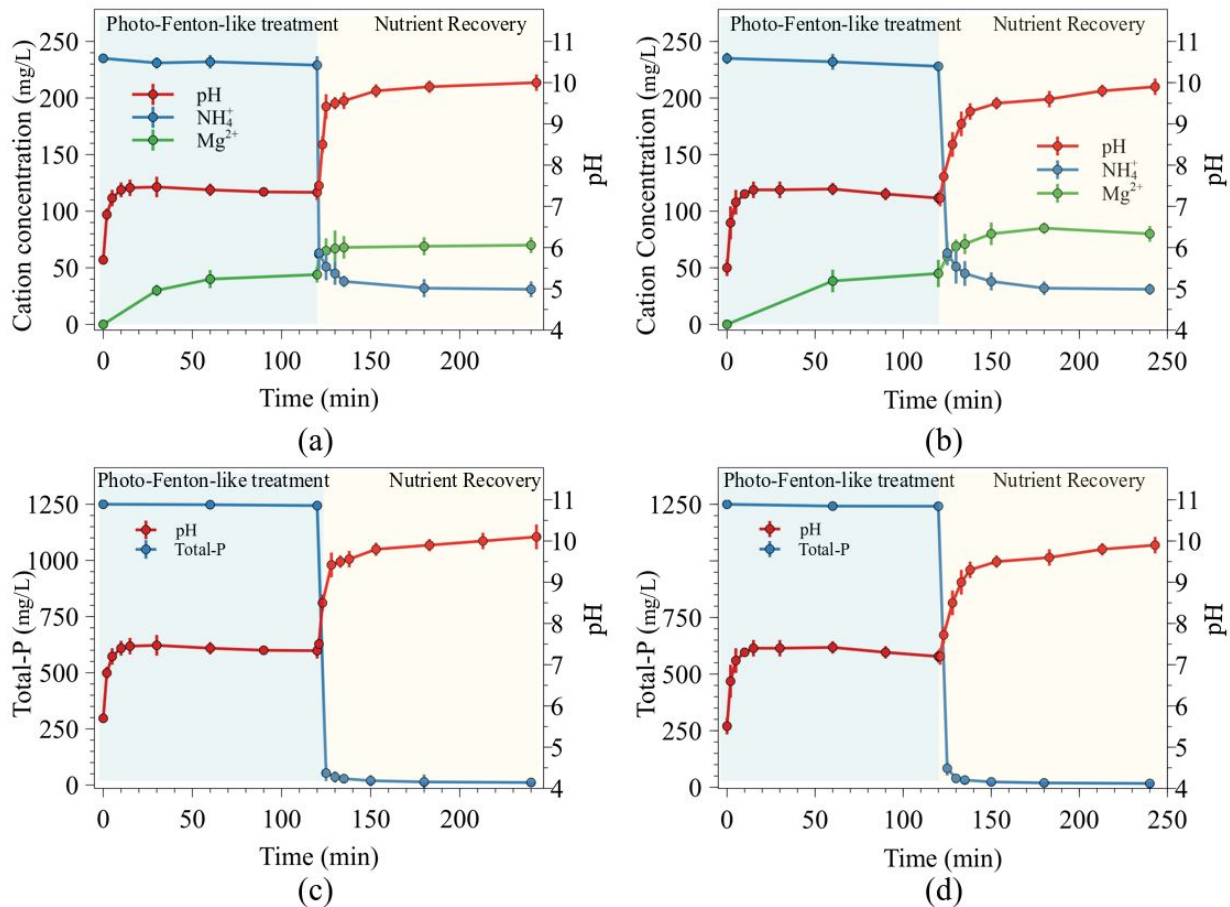
386 **3.6 Tandem photo-Fenton-like oxidation of ECs and subsequent nutrient recovery**

387 As previous sections have established that 1) ECs can incorporate into struvite during direct
388 nutrient capture with no EC oxidation (shown in Figure 4) 2) the Cu-MgO catalyst can potentially
389 oxidize the ECs to linear acids with no toxicity risks (**Section 3.5**), a tandem process of oxidizing
390 the ECs first and then recovering nutrients via struvite crystallization is proposed. For Stage 1
391 where the Fenton oxidation occurs, a 250 mg/L loading of Cu-MgO is used, as SI calculations
392 show this would not lead to struvite crystallization as the solution remains undersaturated, but the
393 catalyst provides sufficient activity to oxidize ECs. Following catalyst separation, Stage 2 utilizes
394 750 mg/L undoped MgO to initiate struvite recovery, as the pH increase from MgO dissolution
395 and the increased concentration of MgO provides the correct SI for struvite formation (highlighted
396 Stage 2 area in Figure 3(a)). The cation and anion concentration, as well as the solution pH, are
397 shown in Figure 7 for the tandem process where the first 120 minutes show the ion concentrations
398 and pH overtime for the Fenton oxidation step (plot area highlighted in blue), and the subsequent
399 120 minutes are for struvite recovery which occurs after the catalyst is removed and undoped MgO
400 is added to the solution. As shown in Figure 7, the PO_4^{3-} and NH_4^+ concentrations remain constant

401 over the photo-Fenton-like oxidation stage. In both cases of p-OXN and TCL, the pH increases
402 rapidly in the first 15 minutes following the addition of the Cu-MgO catalyst due to the surface
403 hydration of the MgO support.^{48,67} Previous work on MgO has shown that water diffuses into the
404 pores and hydrates the surface to produce $\text{Mg}(\text{OH})^+_{(\text{surface})}$ and $\text{OH}^-_{(\text{aq})}$, which causes the pH to
405 rise.^{48,68} The $\text{Mg}(\text{OH})^+_{(\text{surface})}$ and Mg^{2+} ions close to the surface, recombine with OH^- to produce
406 an overlayer of $\text{Mg}(\text{OH})_2$, which terminates further dissolution of the surface and stabilizes the pH
407 in the range of 7.2-7.5 in this study.^{48,68,69} Overtime slight depression of the pH is observed due to
408 dissolution of CO_2 from the atmosphere, but this effect is not significant over short periods.⁴⁸ The
409 second pH rise occurs due to the addition of undoped MgO, which acts as the Mg-source for
410 struvite precipitation. Since the second phase uses a slight excess of MgO, an immediate decrease
411 in PO_4^{3-} and NH_4^+ concentrations due to struvite formation. The pH in the second phase rises to
412 the range from the range of 7.2-7.5 to the range of 9.3-9.8 in the first 15 minutes following MgO
413 addition and attains a final pH of 9.9-10.

414 The pH control provided by the MgO support dissolution during the photo-Fenton-like oxidation
415 stage provides the important advantage of preventing Cu from leaching into the aqueous phase.⁴⁵
416 During the second phase which is nutrient recovery, the increased pH is necessary to induce
417 struvite precipitation, as the typical pH range of 7 – 9.5 is required.^{18,51,70} Figures 7(a) and (b)
418 depict the cation concentrations and the pH over the reaction time. At the end of the 2-hour nutrient
419 recovery phase, 87% NH_4^+ removal was observed in both cases where p-OXN and TCL were
420 pretreated with the photo-Fenton-like reaction. The residual Mg^{2+} concentration after the 2-hour
421 struvite recovery phase in the p-OXN case was 70 mg/L, while the TCL case showed 80 mg/L.
422 Figures 7(c) and (d) show the Total-P concentration and the pH of the solution over the reaction
423 time. After the 2-hour reaction time, both the p-OXN and TCL pretreated experiments yielded

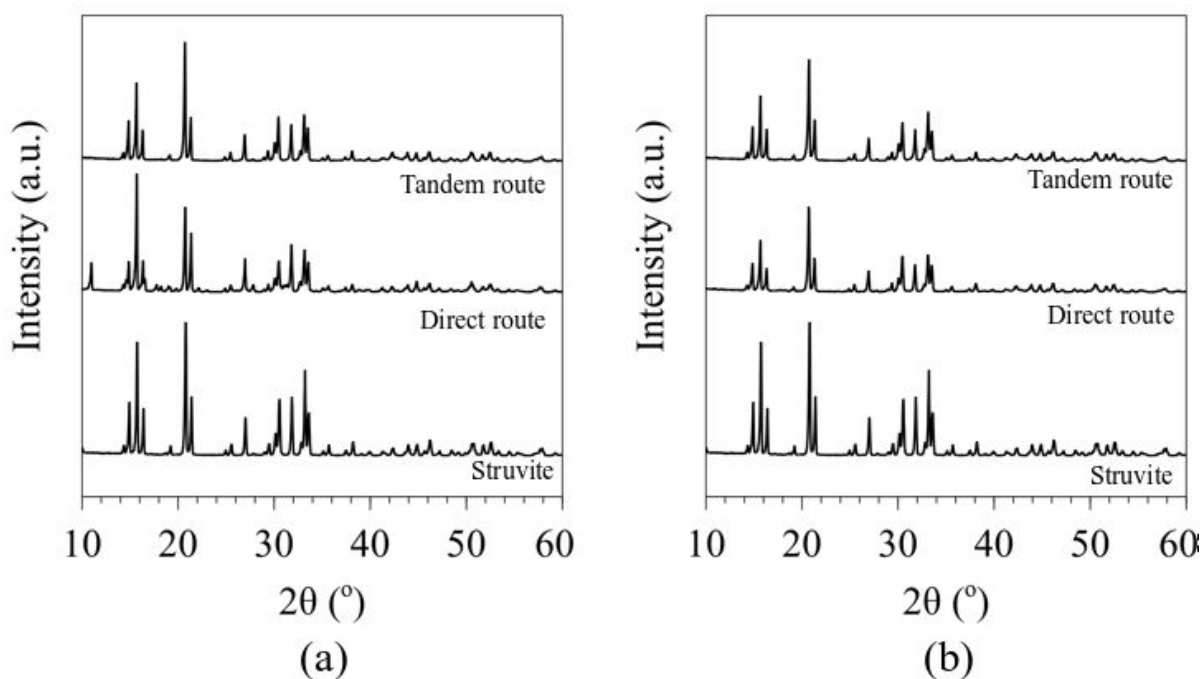
424 99% total-P removal. This total-P removal is consistent with previous work on mesoporous MgO.²⁰
 425 Compared to microcrystalline MgO, the rate of adsorption is highly enhanced in mesoporous MgO
 426 due to the faster intraparticle diffusion facilitated by the mesopore structure.^{18,20} Previous work on
 427 MgO supported on porous supports such as diatomite has also demonstrated similar enhanced
 428 kinetics, but with the disadvantage of incorporating the support in the struvite product.^{70,71}



429
 430 Figure 7. Cation (NH₄⁺ and Mg²⁺) concentrations (mg/L) and pH of the solution as a function of
 431 time during the tandem AOP and nutrient recovery process with (a) p-OXN (b) TCL. Total-P
 432 concentration (mg/L) and pH of the solution as a function of time during tandem AOP and
 433 nutrient recovery process with (c) p-OXN (d) TCL.

434 3.7 Struvite Product Physicochemical Characterization

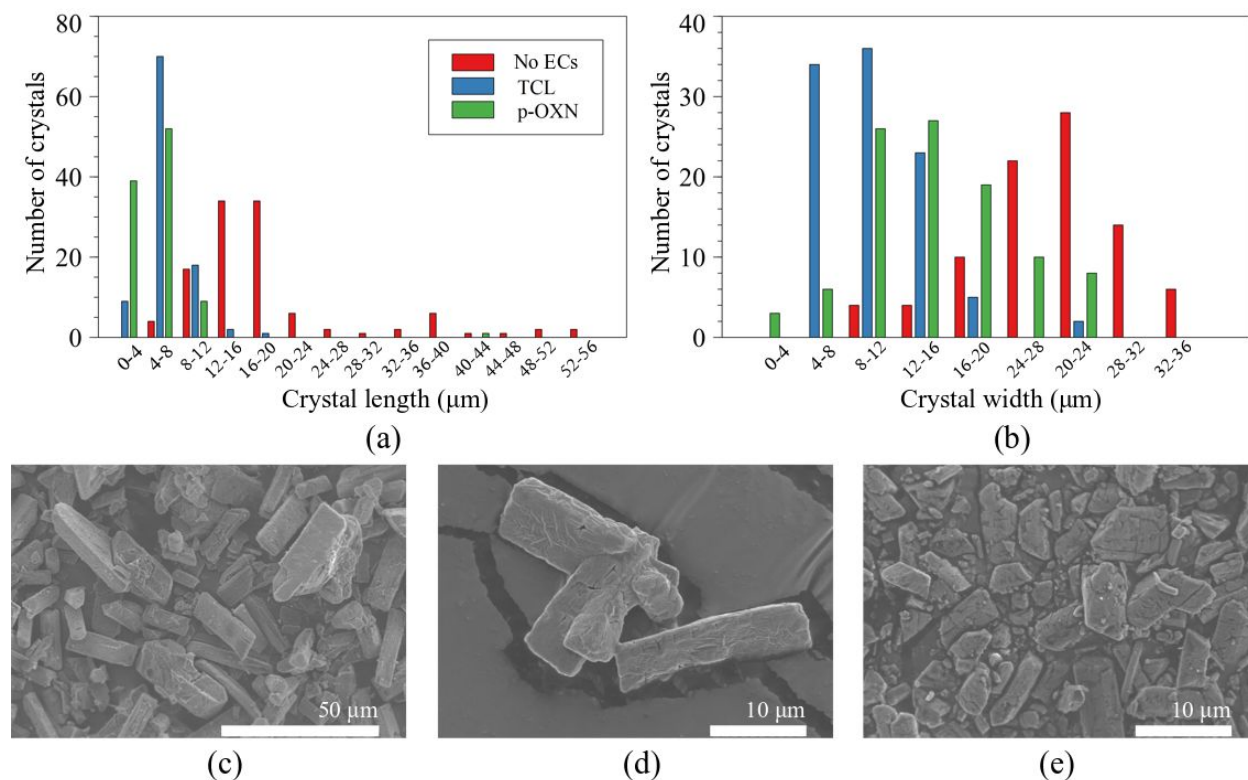
435 The crystal structure of the produced struvite samples was studied using powder XRD. Figure 8
436 shows the XRD patterns for struvite formed without any ECs, struvite recovered in the presence
437 of ECs (direct nutrient capture route), and struvite recovered using the tandem route. In all cases
438 the dominant XRD pattern was the struvite pattern, indicating that the major crystalline product is
439 struvite (PDF#15-0762).⁷² This has been demonstrated to be the case in previous work using both
440 mesoporous MgO NPs and microcrystalline MgO.^{18,20} As shown in Figure 8(a), the XRD patterns
441 for struvite formed in the presence of p-OXN, and the struvite formed following the photo-Fenton-
442 like catalytic oxidation contain a minor peak at 11°. This peak is attributed to a small quantity of
443 $\text{Mg}_3(\text{PO}_4)_2 \cdot 22\text{H}_2\text{O}$ present (PDF#35-0186) in struvite. At high pH and high concentrations of PO_4^{3-}
444 the formation of $\text{Mg}_3(\text{PO}_4)_2 \cdot 22\text{H}_2\text{O}$ becomes thermodynamically stable as shown by SI
445 calculations, which leads to the crystalline product being a mixture of struvite and
446 $\text{Mg}_3(\text{PO}_4)_2 \cdot 22\text{H}_2\text{O}$, with $\text{Mg}_3(\text{PO}_4)_2 \cdot 22\text{H}_2\text{O}$ being the minor product.



447

448 Figure 8. XRD patterns for struvite formed using the (a) Direct route in the presence of p-oxN
449 and the tandem route (b) Direct route in the presence of TCL and the tandem route

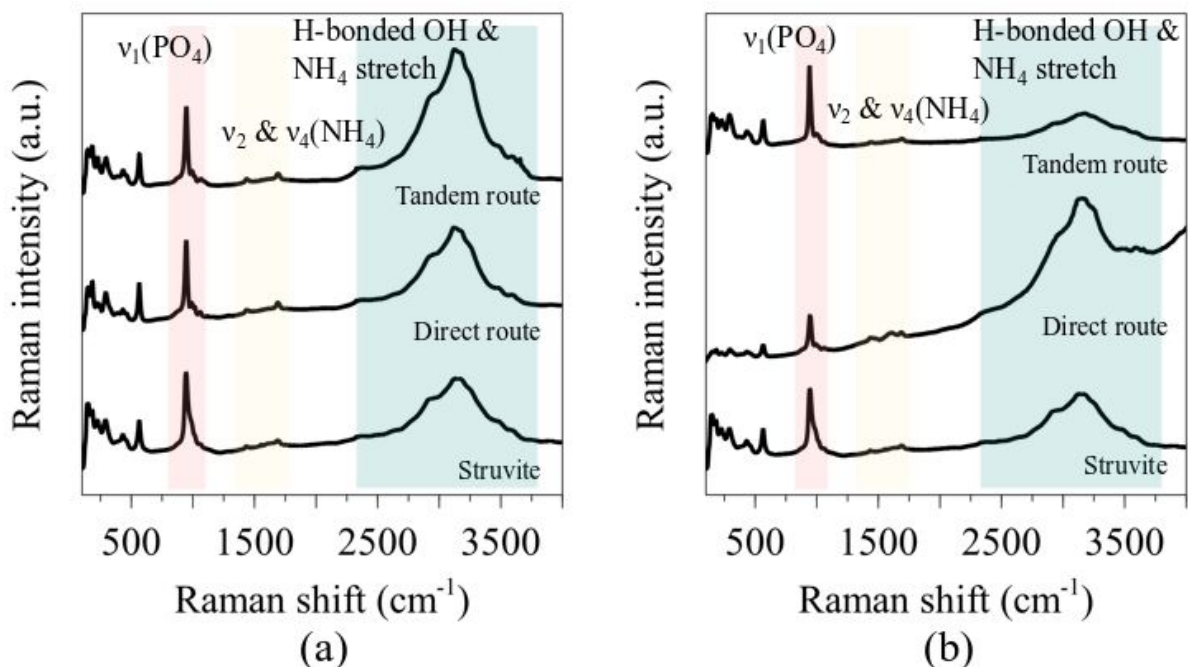
450 Figure 9 shows select SEM images and size distributions for the struvite crystals formed in the
451 presence of the ECs using the direct nutrient capture route. The purpose of the size distribution
452 analysis of struvite crystals formed in the presence of ECs was to identify whether the distribution
453 crystal lengths and widths would be altered due to the presence of ECs. As shown in Figure 9(a)
454 and (b), the average crystal length and width are reduced in the presence of ECs. The production
455 of smaller crystals in the presence of dissolved organic matter has been reported in previous
456 literature.⁵¹ The N release rate from struvite is dependent on crystal size in the initial 6 weeks after
457 application, with smaller crystals releasing more N due to higher exposed surface area.^{73,74}
458 Therefore, controlling struvite crystal size has important implications on its application, and thus,
459 producing struvite in a solution with less organic matter would be beneficial. The characteristic
460 rod-shaped struvite crystals are present in the SEM images shown in Figures 9(c)-(e).



461
 462 Figure 9. Size histograms for struvite crystals in the presence of organic contaminants (a) crystal
 463 length (b) crystal width. Select SEM images for (c) Struvite formed with no ECs present (d)
 464 struvite formed using the direct route in the presence of p-OXN (e) struvite formed using the direct
 465 route in the presence of TCL (histogram generated using measurements from 100 individual
 466 crystals).

467 Raman spectra for the produced struvite crystals are shown in Figure 10. In all three cases, the
 468 major struvite peaks were evident, confirming the XRD finding that struvite is the major crystalline
 469 product for each scenario. Figure 10(a) shows the Raman spectra for the control struvite sample,
 470 struvite formed in the presence of p-OXN, and the struvite formed following the Fenton oxidation
 471 of the solution containing p-OXN. All three spectra show the same major peak positions. Figure
 472 10(b) shows the Raman spectra for the control struvite sample, struvite formed in the presence of
 473 TCL, and the struvite formed following the Fenton oxidation of the solution containing TCL. In

474 all cases the $\nu_1(\text{PO}_4)$ stretch for struvite is located at 946 cm^{-1} , while the ν_4 mode corresponds to
475 560 cm^{-1} .^{75,76} The hydrogen-bonded hydroxyl/water and ammonium species lead to the rise of a
476 prominent region, with broadband centered around 3124 cm^{-1} and a shoulder around 2950 cm^{-1} .^{77,78}
477 Struvite contains tetrahedral NH_4^+ groups, as evidenced by the 1435 cm^{-1} and 1690 cm^{-1} peaks.^{77,78}
478 The struvite sample formed in the presence of TCL showed laser-induced fluorescent behavior
479 during analysis, resulting in a sloping baseline. Such fluorescence can be observed due to
480 chromophores in the sample that are excited to a higher electronic state such as the conjugated
481 rings of TCL adsorbed on the struvite crystals, which results in radiation emitted that is larger than
482 that of the Raman signal of interest.⁷⁹ Previous literature on struvite synthesis in the presence of
483 ECs such as TCL has shown that the contaminant can incorporate into or adsorb onto the struvite
484 crystal to varying degrees depending on the exact chemical identity of the ECs.^{28,80} The struvite
485 samples formed in the presence of p-OXN remained the white color observed in the control sample
486 as the p-OXN solution was colorless, while the struvite synthesized in the presence of TCL
487 obtained the orange color present in the TCL solution. While the Raman spectrum for the struvite
488 containing TCL contained largely the same major peaks present in the pure struvite, one additional
489 minor peak was evident at 1603 cm^{-1} was observed. This peak has been assigned in literature to C-
490 C stretches as well as C-O bends and is the major TCL peak in the $1700\text{-}600\text{ cm}^{-1}$ region.⁸¹⁻⁸³
491 Other TCL peaks in this region have very low intensities, and as such, were not detected in this
492 analysis.^{81,83} Therefore, the 1603 cm^{-1} peak is not definitively assigned to TCL in this work. The
493 low concentration of adsorbed ECs provides low-intensity signals which are easily overcome by
494 the higher intensity of Raman signal coming from the crystalline struvite, and thus, detecting
495 adsorbed ECs using Raman spectroscopy becomes challenging.



496

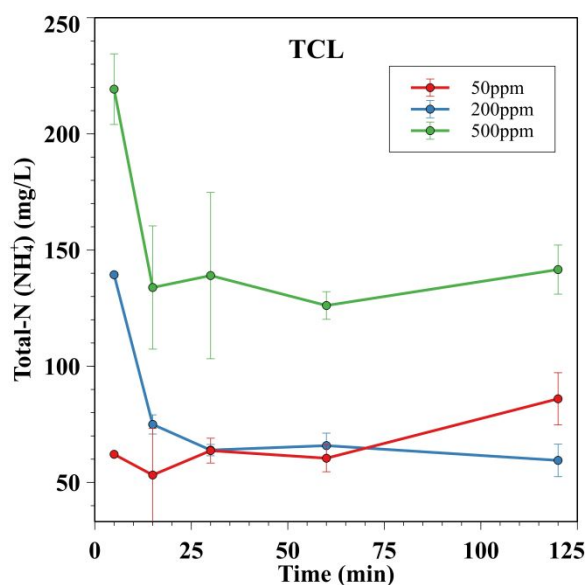
497 Figure 10. Raman spectra for struvite (a) with p-OXN and post-Fenton oxidation (b) with TCL

498 and post-Fenton oxidation

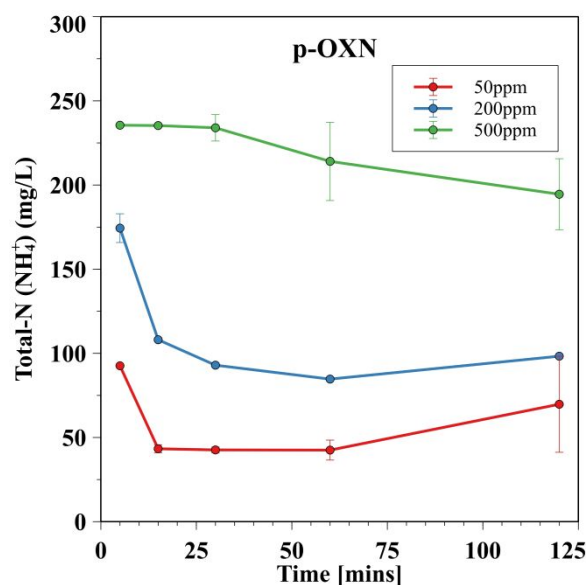
499 3.8 Ca²⁺ Concentration Effects on NH₄⁺ Adsorption and the Resulting Solid Product 500 Formation

501 Finally, we investigated the Ca²⁺ ion, commonly found in wastewater, effects on NH₄⁺ ion removal
 502 during the nutrient recovery phase in a 2-step process using TCL and p-OXN post-Fenton
 503 oxidation solution. In Figures 11a and b, it can be seen that for both TCL and p-OXN NH₄⁺ ion
 504 removal directly correlates with Ca²⁺ concentration in an aqueous solution. In particular,
 505 increasing Ca²⁺ concentration decreases NH₄⁺ ion removal. The apparent reason for this
 506 phenomenon can be inferred from Figure 11c where a complex mixture of the solid product was
 507 obtained using XRD, differently from Figure 8 where only struvite was observed. Two additional
 508 observations can be made from Figure 11c. A non-struvite peak at $\sim 2\theta = 11^\circ$ transitioned to 12°
 509 with the increasing Ca²⁺ content. Additionally and somewhat unexpectedly, the complex mixture

510 of the solid products changed with the increasing Ca^{2+} content to that of pure struvite shown in
511 Figure 8 and a strong peak due to the hydrated magnesium phosphate at $\sim 2\theta=12^\circ$. This
512 improvement in the observed struvite crystallinity is also observed in Figure 11d where a strong
513 $2\theta=12^\circ$ peak is complemented by a minor struvite amount since the adsorption of NH_4^+ , as shown
514 in Figure 11b, decreases at 500 ppm Ca^{2+} . Figure 11 suggests that Ca^{2+} has a significant effect on
515 NH_4^+ adsorption from post-Fenton oxidation solutions using 750 mg/L of MgO NPs with the chief
516 product shifting to magnesium phosphate. Notably, the peak at $2\theta=12^\circ$ could not be associated
517 with any major calcium solids, such as CaCO_3 or $\text{Ca}(\text{OH})_2$.



(a)



(b)

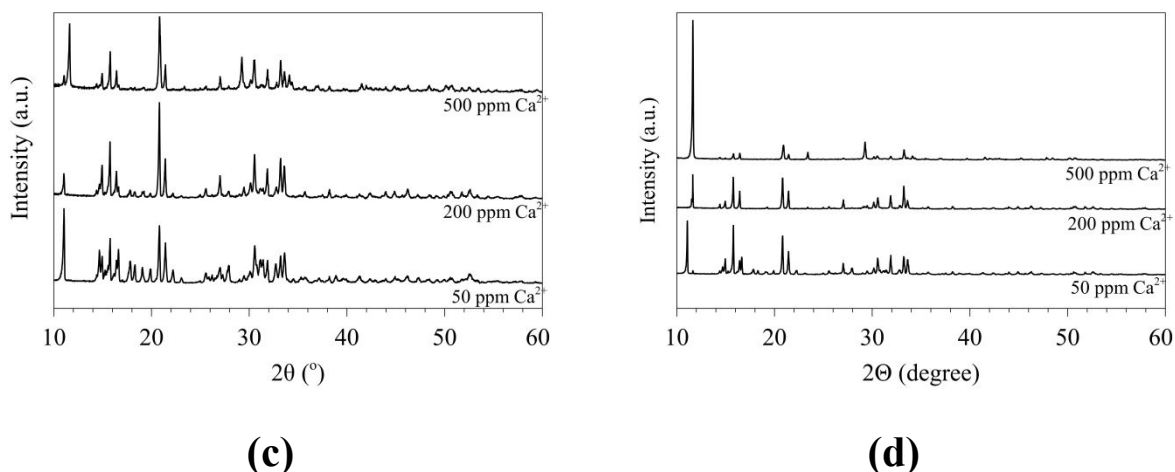


Figure 11. Aqueous NH_4^+ ion composition profile for (a) TCL and (b) p-OXN post-Fenton oxidation during the nutrient recovery phase in the 2-step process shown in Figure 1 with 750 mg/L of MgO NPs added to the solution to initiate struvite formation. In (c) XRD patterns are shown for the solid products as a function of Ca^{2+} concentration resulting from (a) while in (d) – from (b). CaCl_2 was added as calcium source at 50, 200 and 500 ppm Ca^{2+} .

518

519 **4 Conclusions**

520 Struvite recovery provides a unique opportunity to remove nutrients from wastewater that would
 521 cause eutrophication and produce a value-added chemical that can be used as a green fertilizer.
 522 However, the presence of ECs in water has introduced an additional challenge to struvite recovery,
 523 given that these contaminants can adsorb on the struvite crystals and cause various environmental
 524 issues during field application. Both p-OXN and TCL were shown to adsorb on struvite crystals
 525 up to 13% and 37% when struvite was produced directly from wastewater containing these two
 526 ECs, illustrating the importance of eliminating ECs from wastewater before nutrient recovery. This
 527 study shows a tandem process in treating the ECs in nutrient-laden wastewater with a photo-
 528 Fenton-like reaction step as a pretreatment before nutrient recovery *via* struvite crystallization, to

529 extract nutrients in the form of a green fertilizer without the risk of EC incorporation. The photo-
530 Fenton-like reaction using a Cu-MgO catalyst was shown to be effective in eliminating the parent
531 structures of p-OXN and TCL, reducing the risk of toxicity. Using equilibrium modeling, the Cu-
532 MgO catalyst loading was chosen to achieve sufficient activity, while ensuring the solution
533 remains undersaturated, preventing struvite precipitation. Following the Fenton oxidation stage
534 and catalyst separation, the nutrient recovery was conducted by adding undoped MgO, the loading
535 of which was guided by the SI calculations to selectively produce struvite as the major crystalline
536 product. Product characterization using XRD and Raman revealed that struvite is produced as the
537 major product and that while struvite and $Mg_3PO_4 \cdot 22H_2O$ were both predicted to precipitate by
538 equilibrium modeling, struvite forms as a kinetically favored product. SEM analysis showed that
539 the particle size distribution of struvite is altered by ECs, as struvite formed in the presence of ECs
540 yielded finer crystals.

541 **Conflicts of Interest.** The authors declare no conflicts of interest.

542 **Acknowledgments.** This material is based upon work supported by the National Science
543 Foundation under Grant No. CHE 1710120. The authors acknowledge Dr. Bar Mosevitzky Lis for
544 assistance in obtaining Raman data.

545 **References**

- 546 1 J. A. Foley, R. Defries, G. P. Asner, C. Barford, G. Bonan, S. R. Carpenter, F. S. Chapin,
547 M. T. Coe, G. C. Daily, H. K. Gibbs, J. H. Helkowski, T. Holloway, E. A. Howard, C. J.
548 Kucharik, C. Monfreda, J. A. Patz, I. C. Prentice, N. Ramankutty and P. K. Snyder, 2005,
549 **8**, 570–574.
- 550 2 J. A. Foley, N. Ramankutty, K. A. Brauman, E. S. Cassidy, J. S. Gerber, M. Johnston, N.
551 D. Mueller, C. O’Connell, D. K. Ray, P. C. West, C. Balzer, E. M. Bennett, S. R.
552 Carpenter, J. Hill, C. Monfreda, S. Polasky, J. Rockström, J. Sheehan, S. Siebert, D.
553 Tilman and D. P. M. Zaks, *Nature*, 2011, **478**, 337.
- 554 3 J. N. Galloway, A. R. Townsend, J. W. Erisman, M. Bekunda, Z. Cai, J. R. Freney, L. A.
555 Martinelli, S. P. Seitzinger and M. A. Sutton, *Science (80-.)*, 2008, **320**, 889–892.
- 556 4 B. E. Rittmann, B. Mayer, P. Westerhoff and M. Edwards, *Chemosphere*, 2011, **84**, 846–
557 853.
- 558 5 J. N. Galloway and E. B. Cowling, *AMBIO A J. Hum. Environ.*, 2002, **31**, 64–71.
- 559 6 J. N. Galloway, J. D. Aber, J. W. Erisman, S. P. Seitzinger, R. W. Howarth, E. B. Cowling
560 and B. J. Cosby, *Bioscience*, 2003, **53**, 341–356.
- 561 7 J. Baltrusaitis, *ACS Sustain. Chem. Eng.*, 2017, **5**, 9527–9527.
- 562 8 D. E. Canfield, A. N. Glazer and P. G. Falkowski, *Science*, 2010, **330**, 192–6.
- 563 9 J. J. Beaulieu, T. DelSontro and J. A. Downing, *Nat. Commun.*, 2019, **10**, 1375.
- 564 10 M. Silva and J. Baltrusaitis, *Environ. Sci. Water Res. Technol.*, 2020, **6**, 3178–3194.
- 565 11 B. K. Mayer, L. A. Baker, T. H. Boyer, P. Drechsel, M. Gifford, M. A. Hanjra, P.
566 Parameswaran, J. Stoltzfus, P. Westerhoff and B. E. Rittmann, *Environ. Sci. Technol.*,
567 2016, **50**, 6606–6620.
- 568 12 T. Cai, S. Y. Park and Y. Li, *Renew. Sustain. Energy Rev.*, 2013, **19**, 360–369.
- 569 13 M. Smol, *J. Mater. Cycles Waste Manag.*, 2019, 21, 227–238.
- 570 14 H. P. Jing, Y. Li, X. Wang, J. Zhao and S. Xia, *Environ. Sci. Water Res. Technol.*, 2019,

- 571 5, 931–943.
- 572 15 P. Kehrein, M. van Loosdrecht, P. Osseweijer, M. Garfi, J. Dewulf and J. Posada,
573 *Environ. Sci. Water Res. Technol.*, 2020, **6**, 877–910.
- 574 16 M. Silva, J. P. Baltrus, D. J. Burnett and J. Baltrusaitis, *ACS Earth Sp. Chem.*, 2022, **6**,
575 431–443.
- 576 17 Y. Luo, H. Li, Y.-R. Huang, T.-L. Zhao, Q.-Z. Yao, S.-Q. Fu and G.-T. Zhou, *Chem. Eng.*
577 *J.*, 2018, **351**, 195–202.
- 578 18 D. Kiani, Y. Sheng, B. Lu, D. Barauskas, K. Honer, Z. Jiang and J. Baltrusaitis, *ACS*
579 *Sustain. Chem. Eng.*, 2018, **7**, 1545–1556.
- 580 19 N. Park, H. Chang, Y. Jang, H. Lim, J. Jung and W. Kim, *Water Sci. Technol.*, 2020, **81**,
581 2511–2521.
- 582 20 M. Silva, V. Murzin, L. Zhang, J. P. Baltrus and J. Baltrusaitis, *Environ. Sci. Nano*, 2020,
583 **7**, 3482–3496.
- 584 21 B. Lu, D. Kiani, W. Taifan, D. Barauskas, K. Honer, L. Zhang and J. Baltrusaitis, *J. Phys.*
585 *Chem. C*, 2019, **123**, acs.jpcc.8b12252.
- 586 22 D. Kiani, M. Silva, Y. Sheng and J. Baltrusaitis, *J. Phys. Chem. C*, 2019, **123**, 25135–
587 25145.
- 588 23 J. Pesonen, P. Myllymäki, S. Tuomikoski, G. Vervecken, T. Hu, H. Prokkola, P. Tynjälä,
589 U. Lassi, J. Pesonen, P. Myllymäki, S. Tuomikoski, G. Vervecken, T. Hu, H. Prokkola, P.
590 Tynjälä and U. Lassi, *ChemEngineering*, 2019, **3**, 40.
- 591 24 L. Chen, C. H. Zhou, H. Zhang, D. S. Tong, W. H. Yu, H. M. Yang and M. Q. Chu,
592 *Chemosphere*, 2017, **187**, 302–310.
- 593 25 U. J. Kim, J. K. Oh and K. Kannan, *Environ. Sci. Technol.*, 2017, **51**, 7872–7880.
- 594 26 Q. Zhang, S. Zhao, X. Ye and W. Xiao, *Desalin. Water Treat.*, 2016, **57**, 10924–10933.
- 595 27 A. Rabinovich and A. A. Rouff, *ACS ES&T Water*, 2021, **1**, 910–918.
- 596 28 Z. L. Ye, Y. Deng, Y. Lou, X. Ye, J. Zhang and S. Chen, *Chem. Eng. J.*, 2017, **313**, 1633–

- 597 1638.
- 598 29 Q. L. Chen, X. L. An, Y. G. Zhu, J. Q. Su, M. R. Gillings, Z. L. Ye and L. Cui, *Environ.*
599 *Sci. Technol.*, 2017, **51**, 8149–8157.
- 600 30 M. A. De Boer, C. Kabbe and J. C. Slootweg, *Environ. Sci. Technol.*, 2018, **52**, 14564–
601 14565.
- 602 31 T. G. Bekele, H. Zhao, Q. Wang and J. Chen, *Environ. Sci. Technol.*, 2019, **53**, 13417–
603 13426.
- 604 32 A. Blum, M. Behl, L. S. Birnbaum, M. L. Diamond, A. Phillips, V. Singla, N. S. Sipes, H.
605 M. Stapleton and M. Venier, *Environ. Sci. Technol. Lett.*, 2019, **6**, 638–649.
- 606 33 A. K. Greaves and R. J. Letcher, *Environ. Sci. Technol.*, 2014, **48**, 7942–7950.
- 607 34 Q. Zhang, Y. Yao, Y. Wang, Q. Zhang, Z. Cheng, Y. Li, X. Yang, L. Wang and H. Sun,
608 *Environ. Pollut.*, 2021, **288**, 117742.
- 609 35 L. Y. Kuo and N. M. Perera, *Inorg. Chem.*, 2000, **39**, 2103–2106.
- 610 36 L. Poirier, L. Plener, D. Daudé and E. Chabrière, *Sci. Reports 2020 101*, 2020, **10**, 1–11.
- 611 37 C. Pope, *Encycl. Toxicol. Third Ed.*, 2014, 759–761.
- 612 38 G. A. Petroianu, M. Y. Hasan, K. Arafat, S. M. Nurulain and A. Schmitt, *J. Appl. Toxicol.*,
613 2005, **25**, 562–567.
- 614 39 W. Y. Xie, Q. Shen and F. J. Zhao, *Eur. J. Soil Sci.*, 2018, **69**, 181–195.
- 615 40 J. Rivera-Utrilla, M. Sánchez-Polo, M. Á. Ferro-García, G. Prados-Joya and R. Ocampo-
616 Pérez, *Chemosphere*, 2013, **93**, 1268–1287.
- 617 41 K. E. O’Shea and D. D. Dionysiou, *J. Phys. Chem. Lett.*, 2012, **3**, 2112–2113.
- 618 42 Y. Zhu, R. Zhu, Y. Xi, J. Zhu, G. Zhu and H. He, *Appl. Catal. B Environ.*, 2019, **255**,
619 117739.
- 620 43 M. Silva and J. Baltrusaitis, *J. Hazard. Mater. Lett.*, 2021, **2**, 100012.
- 621 44 E. Yamal-Turbay, E. Jaén, M. Graells and M. Pérez-Moya, *J. Photochem. Photobiol. A*

- 622 *Chem.*, 2013, **267**, 11–16.
- 623 45 M. Silva, J. P. Baltrus, C. Williams, A. Knopf, L. Zhang and J. Baltrusaitis, *Appl. Catal. A*
624 *Gen.*, 2022, **630**, 118468.
- 625 46 S. Xin, G. Liu, X. Ma, J. Gong, B. Ma, Q. Yan, Q. Chen, D. Ma, G. Zhang, M. Gao and
626 Y. Xin, *Appl. Catal. B Environ.*, 2021, **280**, 119386.
- 627 47 J. Feng, X. Hu and L. Y. Po, *Environ. Sci. Technol.*, 2004, **38**, 5773–5778.
- 628 48 P. Stolzenburg, A. Capdevielle, S. Teychené and B. Biscans, *Chem. Eng. Sci.*, 2015, **133**,
629 9–15.
- 630 49 S. K. L. Ishii and T. H. Boyer, *Water Res.*, 2015, **79**, 88–103.
- 631 50 T. Zhang, L. Ding and H. Ren, *J. Hazard. Mater.*, 2009, **166**, 911–915.
- 632 51 M. M. Rahman, M. A. M. Salleh, U. Rashid, A. Ahsan, M. M. Hossain and C. S. Ra,
633 *Arab. J. Chem.*, 2014, **7**, 139–155.
- 634 52 Y. S. Ho and G. McKay, *Process Biochem.*, 1999, **34**, 451–465.
- 635 53 J. P. Gustafsson, 2011, 1–73.
- 636 54 M. Silva, J. Baltrus, C. Williams, A. Knopf, L. Zhang and J. Baltrusaitis, *J. Environ.*
637 *Chem. Eng.*, 2021, **9**, 105589.
- 638 55 M. Fang, R. Zheng, Y. Wu, D. Yue, X. Qian, Y. Zhao and Z. Bian, *Environ. Sci. Nano*,
639 2019, **6**, 105–114.
- 640 56 G. A. El-Shobaky, M. Mokhtar and A. M. Salem, *Mater. Res. Bull.*, 2005, **40**, 891–902.
- 641 57 H. S. Liu, K. J. Wang, X. Y. Cao, J. X. Su and Z. Gu, *RSC Adv.*, 2021, **11**, 12532–12542.
- 642 58 D. A. Svintsitskiy, T. Y. Kardash, O. A. Stonkus, E. M. Slavinskaya, A. I. Stadnichenko,
643 S. V. Koscheev, A. P. Chupakhin and A. I. Boronin, *J. Phys. Chem. C*, 2013, **117**, 14588–
644 14599.
- 645 59 D. Zhao, C.-M. Tu, X.-J. Hu and N. Zhang, *RSC Adv.*, 2017, **7**, 37596–37603.
- 646 60 S. H. Lee, B. H. Yoo, S. J. Lim, T. H. Kim, S. K. Kim and J. Y. Kim, *J. Cryst. Growth*,

- 647 2013, **372**, 129–137.
- 648 61 C. Fang, T. Zhang, R. Jiang and H. Ohtake, *Sci. Reports 2016 61*, 2016, **6**, 1–10.
- 649 62 R. Khamizov, D. A. Sveshnikova, A. E. Kucherova and L. A. Sinyaeva, *Russ. J. Phys.*
650 *Chem. A*, 2018, **92**, 1451–1460.
- 651 63 Y. Wang, L. Rao, P. Wang, Z. Shi and L. Zhang, *Appl. Catal. B Environ.*, 2020, **262**,
652 118308.
- 653 64 N. Barhoumi, N. Oturan, S. Ammar, A. Gadri, M. A. Oturan and E. Brillas, *Environ.*
654 *Chem. Lett.*, 2017, **15**, 689–693.
- 655 65 M. Pirsaeheb, S. Moradi, M. Shahlaei and N. Farhadian, *New J. Chem.*, 2020, **44**, 17735–
656 17743.
- 657 66 Y. Y. Chen, Y. L. Ma, J. Yang, L. Q. Wang, J. M. Lv and C. J. Ren, *Chem. Eng. J.*, 2017,
658 **307**, 15–23.
- 659 67 V. S. Birchal, S. D. F. Rocha, M. B. Mansur and V. S. T. Ciminelli, *Can. J. Chem. Eng.*,
660 2001, **79**, 507–511.
- 661 68 J. A. Mejias, A. J. Berry, K. Refson and D. G. Fraser, *Chem. Phys. Lett.*, 1999, **314**, 558–
662 563.
- 663 69 G. L. Smithson and N. N. Bakhshi, *Can. J. Chem. Eng.*, 1969, **47**, 508–513.
- 664 70 P. Xia, X. Wang, X. Wang, J. Song, H. Wang and J. Zhang, *Colloids Surfaces A*
665 *Physicochem. Eng. Asp.*, 2016, **506**, 220–227.
- 666 71 J. Li, X. Wang, J. Wang, Y. Li, S. Xia and J. Zhao, *Chem. Eng. J.*, 2019, **362**, 802–811.
- 667 72 R. C. de S. Meira, S. P. A. da Paz and J. A. M. Corrêa, *J. Mater. Res. Technol.*, 2020, **9**,
668 15202–15213.
- 669 73 M. Dindarsafa, A. Khataee, B. Kaymak, B. Vahid, A. Karimi and A. Rahmani, *Ultrason.*
670 *Sonochem.*, 2017, **34**, 389–399.
- 671 74 A. E. Johnston and I. R. Richards, *Soil Use Manag.*, 2003, **19**, 45–49.

- 672 75 M. Markovic, B. O. Fowler and M. S. Tung, *J. Res. Natl. Inst. Stand. Technol.*, 2004, **109**,
673 553.
- 674 76 R. L. Frost, M. L. Weier, W. N. Martens, D. A. Henry and S. J. Mills, *Spectrochim. Acta -*
675 *Part A Mol. Biomol. Spectrosc.*, 2005, **62**, 181–188.
- 676 77 V. Stefov, B. Šoptrajanov, I. Kuzmanovski, H. D. Lutz and B. Engelen, *J. Mol. Struct.*,
677 2005, **752**, 60–67.
- 678 78 D. Sidorczuk, M. Kozanecki, B. Civalleri, K. Pernal and J. Prywer, *J. Phys. Chem. A*,
679 2020, **124**, 8668–8678.
- 680 79 E. Yakubovskaya, T. Zaliznyak, J. Martínez Martínez and G. T. Taylor, *Sci. Rep.*, 2019, **9**,
681 15785.
- 682 80 T. Zhang, C. Fang, P. Li and R. F. Jiang, *Adv. Mater. Res.*, 2014, **955**, 1983–1986.
- 683 81 C. Leypold, M. Reiher, G. Brehm, M. Schmitt, S. Schneider, P. Matousek and M. Towrie,
684 *Phys. Chem. Chem. Phys.*, 2003, **5**, 1149–1157.
- 685 82 M. Muhammad, B. Yan, G. Yao, K. Chao, C. Zhu and Q. Huang, *ACS Appl. Nano Mater.*,
686 2020, **3**, 7066–7075.
- 687 83 J. Zhao, P. Liu, H. Yuan, Y. Peng, Q. Hong and M. Liu, *J. Spectrosc.*, 2016, **2016**,
688 1845237.
- 689